Available online at www.sciencedirect.com

jmr&t Journal of Materials Research and Technology

www.jmrt.com.br

Original Article

Texture evolution and phase transformation of 25Cr-6Mo-5Ni experimental duplex stainless steel during hot and cold rolling

Mohammad Masoumi[a,b,*], *Francisco Evarsito Uchôa Reis*[a], *Mirela Oliveira de Castro*[a], *Miloslav Béres*[a], *Hamilton Ferreira Gomes de Abreu*[a]

[a] *Universidade Federal do Ceará, Centro de Tecnologia, Departamento de Engenharia Metalúrgica e de Materiais, Fortaleza, CE, Brazil*
[b] *Universidade de São Paulo, Escola Politécnica, Departamento de Engenharia Metalúrgica e de Materiais, São Paulo, SP, Brazil*

ARTICLE INFO

Article history:
Received 2 February 2016
Accepted 11 January 2017
Available online 12 April 2017

Keywords:
25Cr-6Mo-5Ni stainless steel
Phase transformation
Texture
Kernel average misorientation

ABSTRACT

An experimental as-cast 25Cr-6Mo-5Ni stainless steel has been solution annealed at 1250 °C and subjected to hot and then cold rolling. X-ray diffraction, optical microscopy and electron backscatter diffraction were used to investigate the effect of hot and cold deformation on the phase transformation and texture evolution. The results revealed that dominant {100}//ND and {110}//ND texture components of martensite is originated by shear strain generated between rolls and sheet surface. The Kernel average misorientation augmented significantly with increased strain and decreased deformation temperature. The internal grain structure becomes more heterogeneous with the dislocation piles up preventing dislocations movement. High localized stresses were developed at grain boundaries due to different deformation of individual grains, which enhanced martensitic transformation in these regions.

1. Introduction

High alloy duplex stainless steels, commonly referred as super duplex, have high corrosion resistance comparable to high Mo content super austenitic steels [1]. Both the super duplex and the super austenitic stainless steels are ranked by an empirical formula that calculates the pitting resistance equivalent number (PRN = %Cr + 3.3% Mo + 20%N) [2]. The super austenitic stainless steels present higher PRN values (45) most because of the higher Mo content ~6 wt.%. Their drawback is a high Ni content, which increases cost significantly. Thus, there is a need for a lower cost alternative, *i.e.* duplex stainless steel with increased Mo content and high PRN values.

* *Corresponding author.*
E-mail: mohammad@alu.ufc.br (M. Masoumi).
http://dx.doi.org/10.1016/j.jmrt.2017.01.001

A suitable balance between chemical composition, processing and post treatment plays significant role in the development of new 25Cr-6Mo-5Ni stainless steel. Some investigations [3–5] reported that higher Mo content increases PRN and improves naphthenic acid corrosion resistance, while the body-centered cubic (BCC) structure restricts the workability. However, the retained austenite can improve the mechanical properties of the steels by strain-induced martensitic transformation. Therefore, the high Mo-Ni stainless steels can be used widely in offshore oil and gas exploration in addition to chemical and petrochemical application due to high resistance to pitting and crevice corrosion, resistance to corrosion fatigue, high strength and good weldability.

In general, ferritic stainless steels have inferior mechanical properties in comparison to austenitic [6]. In contrast, the ferritic stainless steels are considered to resist better to stress corrosion cracking [7]. The 25Cr-6Mo-5Ni stainless steels have a good combination of mechanical properties and corrosion resistance due to their dual crystal structure. The mechanical properties of duplex stainless steels strongly depend on various factors such as microstructure (volume fraction and morphology of retained austenite, grain size), ferritic phase mechanical properties, crystallographic texture, grain boundary and local strain distribution. The retained austenite grains that transform into martensite during deformation increases ductility of material by consumption of stored energy.

Zaid et al. [8] reported that austenite shows dominant brass texture, whereas strong alfa-fiber was developed in ferrite during rolling. Liu et al. [9] studied the plastic deformation mechanism in duplex stainless steel. They discovered deformation heterogeneity in phases and showed that ferrite phase γ-fiber components were more intense during multi-pass hot compressions.

The texture evolution in 25Cr-6Mo-5Ni stainless steels is affected by two mechanisms, plastic deformation and martensitic phase transformation. Although, the preferred crystallographic orientations of both austenite and martensite can play a significant role in the physical and mechanical properties, to date less attention has been paid. Therefore, in this work, the texture evolutions during both hot and cold rolling were investigated as a function of thickness reduction to describe the phase transformation and crystallographic orientation changes. A better understanding of structure changes during deformation is required for proper assessment of service life, cost efficient design and failure analysis.

2. Experimental procedure

The material used in the current study is a modified super 25Cr-6Mo-5Ni stainless steel produced in an electric induction furnace. The chemical composition is listed in Table 1. The experimental as-cast ingot was solution annealed at 1250 °C for 20 min followed by water quenching to prevent the formation of hard and brittle precipitation, *i.e.* Cr-rich phase. In the solution annealed condition, ferritic matrix with retained austenite consisting of both metastable Widmanstätten and blocky austenite was revealed, Fig. 1.

The solution annealed ingot was cut to 6 mm thick sample and subjected to hot rolling at 1250 °C using Stanat model TA-315 rolling machine with the rolling speed of 0.2 ms^{-1} to reach a 50% reduction (t = 3 mm) and was water quenched. Further cold-rolling with 50 and 67% reduction was conducted parallel to the direction of the hot rolling. In this respect, the rolling was performed with the rolling speed of 0.2 ms^{-1} in 15 passes to achieve the final thickness of 1.5 and 1.0 mm, respectively. In this study, for simplicity, samples are referred as 50% and 67% cold rolled.

Then, the volume fraction of retained austenite of all specimens was measured by X-ray diffraction (XRD) technique using Philips X-Pert diffractometer equipped with Cu Kα radiation. Integrated intensities of the {110}, {200}, {211} and {220} peaks of ferrite and the {111}, {200}, {220} and {311} peaks of austenite were used for calculation of volume fraction of retained austenite using X-Pert software.

Macro-texture measurements have been carried out at the surface of the rolled sheets perpendicular to normal direction (ND). Three incomplete pole figures, {110}, {200}, and {211} for ferrite and four {111}, {200}, {220} {311} were measured using Phillips X-Pert goniometer equipped with Cu Kα radiation. The orientation distribution function (ODF) of each sample was determined from the measured pole figures using the MTEX software [10]. Bunge's angles were adopted to describe orientations, and the $\varphi_2 = 45^\circ$ section of Euler space was used to display the computed ODFs.

The electron backscatter diffraction (EBSD) measurements were conducted in a plane perpendicular to the transverse direction of the sheet. EBSD data were acquired using Phillips XL30 scanning electron microscope operating at acceleration voltage of 20 kV, sample tilt angle of 70°, working distance of 12 mm and 0.5 μm step size. HKL Channel 5 software was used to analyze the data. The Kernel average misorientation was calculated from EBSD data to evaluate and map local plastic strain and recrystallization degree in different regions of each sample.

3. Results and discussion

3.1. *X-ray diffraction*

Fig. 2 shows the volume fraction of both the FCC phase (retained austenite) and the BCC phase (containing ferrite and transformed martensite) determined from XRD patterns. In solution annealed condition, volume fraction of retained

Table 1 – Chemical composition (wt.%) of experimental 25Cr-6Mo-5Ni stainless steel.

C	Si	Mn	Ni	Mo	Cr	P	N	Nb + Ti
0.014	1.18	0.58	5.2	6.07	25.1	0.03	0.03	0.09

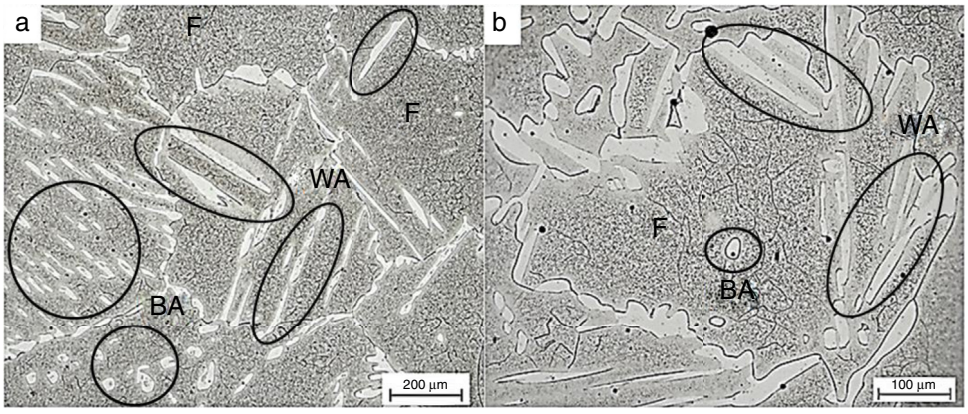

Fig. 1 – Optical micrograph of solution annealed sample at different magnifications (F, ferritic; WA, Widmanstätten austenite; BA, blocky austenite).

austenite was found to be around 33 vol.% with no significant change in hot-rolled condition. With progressing deformation degree at room temperature, the volume fracture of retained austenite decreased from 33 vol.% to 13 and 10 vol.% in 50 and 67% cold rolled specimens, respectively. This reduction in volume fraction can be explained by strain induced martensitic transformation. It is expected that dislocation density increased significantly during cold deformation. Thus separated dislocation walls can enhance transformation of retained austenite into martensite.

3.2. *Texture evolution*

In 25Cr-6Mo-5Ni stainless steels, the retained austenite grains deformed first and transformed into BCC martensite under strain. Recently, Akdut et al. [11] have reported that in duplex stainless steel subjected to deformation the ferrite texture became more isotropic. In austenite however, Brass (110)[112] and Goss (011)[110] texture components were developed. Therefore, in the current work texture evolution during deformation were studied in each phase separately.

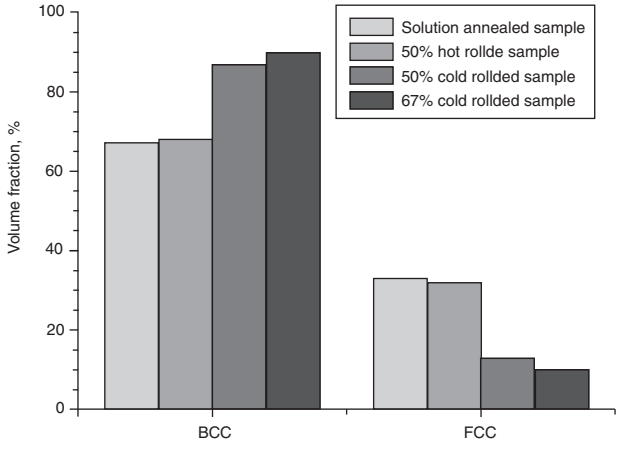

Fig. 2 – Volume fraction of BCC and FCC phases during heat treatment and post deformations determined by XRD technique.

3.2.1. *Austenite texture evolution*

Slip and twinning are the most important mechanisms of plastic deformation in austenite with low stacking fault energy (SFE) [12,13]. In general, slip occurs on the closed packed planes and in the direction of shortest distance between atoms. The crystallographic texture evolution in FCC austenitic phase during hot and cold rolling can be tracked by orientation distribution function (ODF) analysis and is presented in Fig. 3.

Although the ODF intensity was weak in all conditions, the {112}//ND, cube (001)[0$\bar{1}$0], transformed copper (113)[1$\bar{1}$0] and (11$\bar{1}$)[2$\bar{1}$1] components developed in solution heat treated sample, Fig. 3a and b shows the evolution of texture during rolling at 1250 °C. It is observed that the intensity of texture decreased during hot deformation. The (001) $\langle$130$\rangle$ and (110)[1$\bar{1}$3] texture components were developed in this sample. Dynamic recrystallization during hot deformation caused the formation of (001)$\langle$130$\rangle$ components with 20° deflection from ideal cube component. The formation of {110}//ND texture fiber, predominant at close to the Brass (110)$\langle$112$\rangle$ component, was observed and is fully consistent with Refs. [14,15]. The further cold rolling increased intensity of the {001}//ND fiber, with prominent rotated cube (001)$\langle$110$\rangle$ and (001)$\langle$150$\rangle$ components, Fig. 3c. Therefore, strain accumulation during deformation at room temperature is responsible for development of {001}//ND textures. Finally, cube component was dominant in 67% cold rolled samples, Fig. 3d. The absence of Copper (112)$\langle$111$\rangle$ and Brass (110)$\langle$112$\rangle$ components in retained austenite grains of both hot and cold rolled samples is attributed to the absence of shear bands in the deformed matrix.

3.2.2. *Ferrite/martensite texture evolution*

The texture evolution of BCC ferrite/transformed martensite is presented in Fig. 4. In solution treated sample, a dominant (110)[331] texture was observed. The {110}//ND components were characterized with the highest intensity in all investigated specimens, expect in 67% cold rolled samples where {100}//ND fiber was dominant. The {100}//ND components showed a gradual increase with progressing deformation, reached the highest intensity in 67% cold rolled sample. The

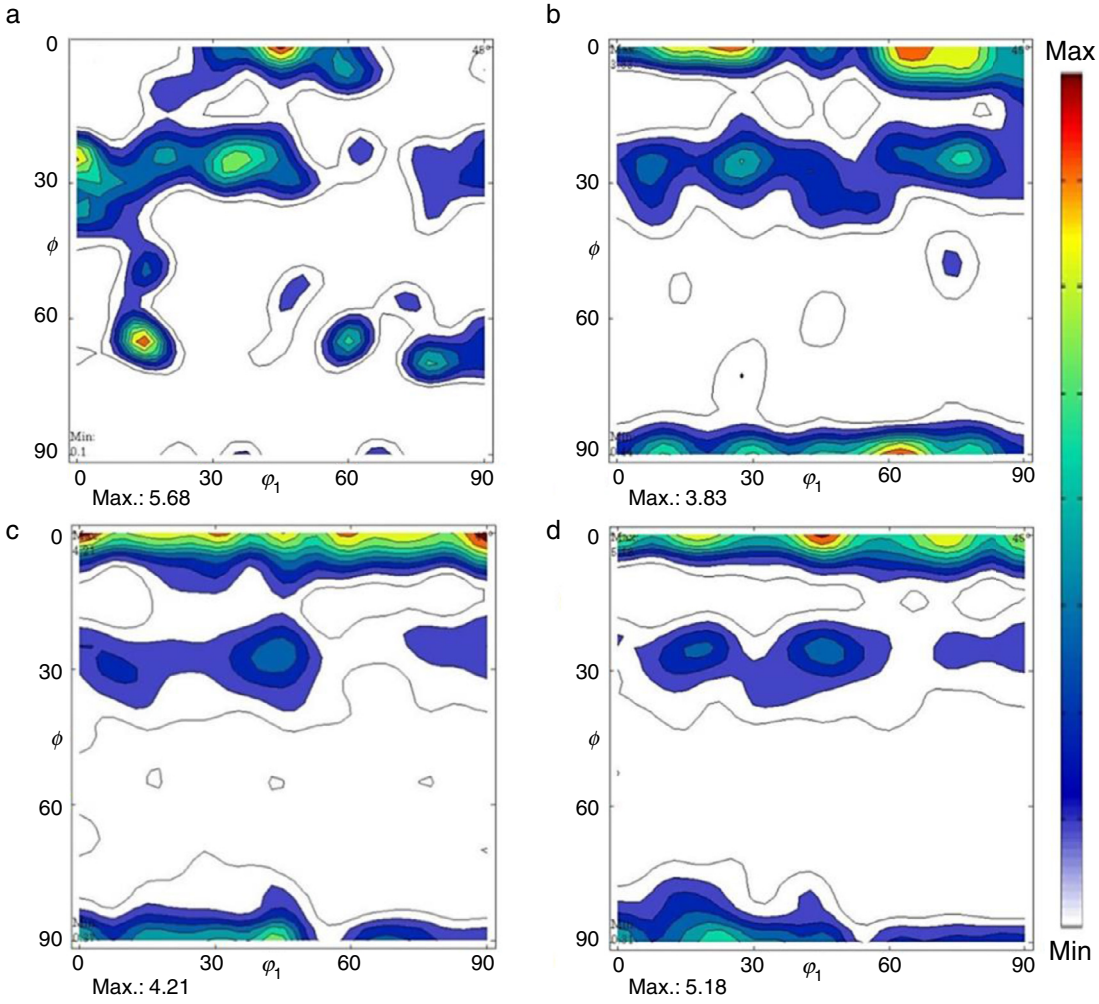

Fig. 3 – ODFs at $\varphi_2 = 45°$, FCC austenite texture evolution of (a) solution heat treated, (b) hot rolled, (c) 50% cold rolled, and (d) 67% cold rolled samples.

{111}//ND fiber texture was weak in all specimens. According to the crystallographic model [16], a BCC lattice can be formed from a FCC lattice by compressing one axis and expanding the other two perpendicular axes. Thus, for the FCC crystal under compression of {100} plane parallel to the rolling direction, the martensite can be developed in the same direction. The texture evolution during cold rolling confirmed that the newly formed BCC grains were aligned with (100) and (110) planes parallel to the normal direction (Fig. 4c and d). It is notable that an increase in {100}//ND ferritic component in cold rolled sample is accompanied with the decreasing in {110}//ND texture in FCC phase [10]. In addition, during cold rolling, available retained austenite at grain interiors was transformed into martensite by specific orientation relationship.

3.2.3. *Selective austenite to martensite transformation*

If the parent austenite phase has a preferred crystallographic orientation, the product phase is also expected to be textured. The elevated temperature during hot rolling promoted the grain boundaries mobility across the {110} and {111} plans. As a result, the {110}//ND texture fiber was developed during hot rolling. Therefore, γ-fiber emerged together with a strong {110}//ND texture during cold rolling. Cube (001)[010] component that developed in austenite after cold deformation has lowest yield strength and therefore a local weakening effect on the plastic properties [17]. This cube (001)[010] texture component of austenite converted to rotated cube (001)[110], (110)[1$\bar{1}$0] rotated Goss and Goss (110)[001] component in ferrite. Therefore, this texture component was intensified at the last deformation process in both BCC and FCC structure.

Fig. 5 shows the correlation between texture components during austenite to martensite transformation, considering 24 variants in Kurdjumov–Sachs (K–S) where {111}γ//{110}α, {110}$_\gamma$//{111}$_\alpha$, are orientation relationships. For example, {100}⟨0$\bar{1}$0⟩ component in austenite can generate {100}⟨1$\bar{1}$0⟩, {100}⟨$\bar{1}\bar{1}$0⟩, {110}⟨1$\bar{1}$0⟩ and {110}⟨001⟩. Since the {100}$<$ 001$>$ component has the highest Taylor factor among all FCC components, it accumulates high dislocation density [18]. Accordingly, during elevated deformation temperature the cube {100}$<$ 001$>$ component is known to be the first to undergo dynamic recrystallization, therefore it disappears because accumulates the highest stored energy [19]. As a consequence, it can enhance austenite to martensite transformation. This can be confirmed when comparing the texture

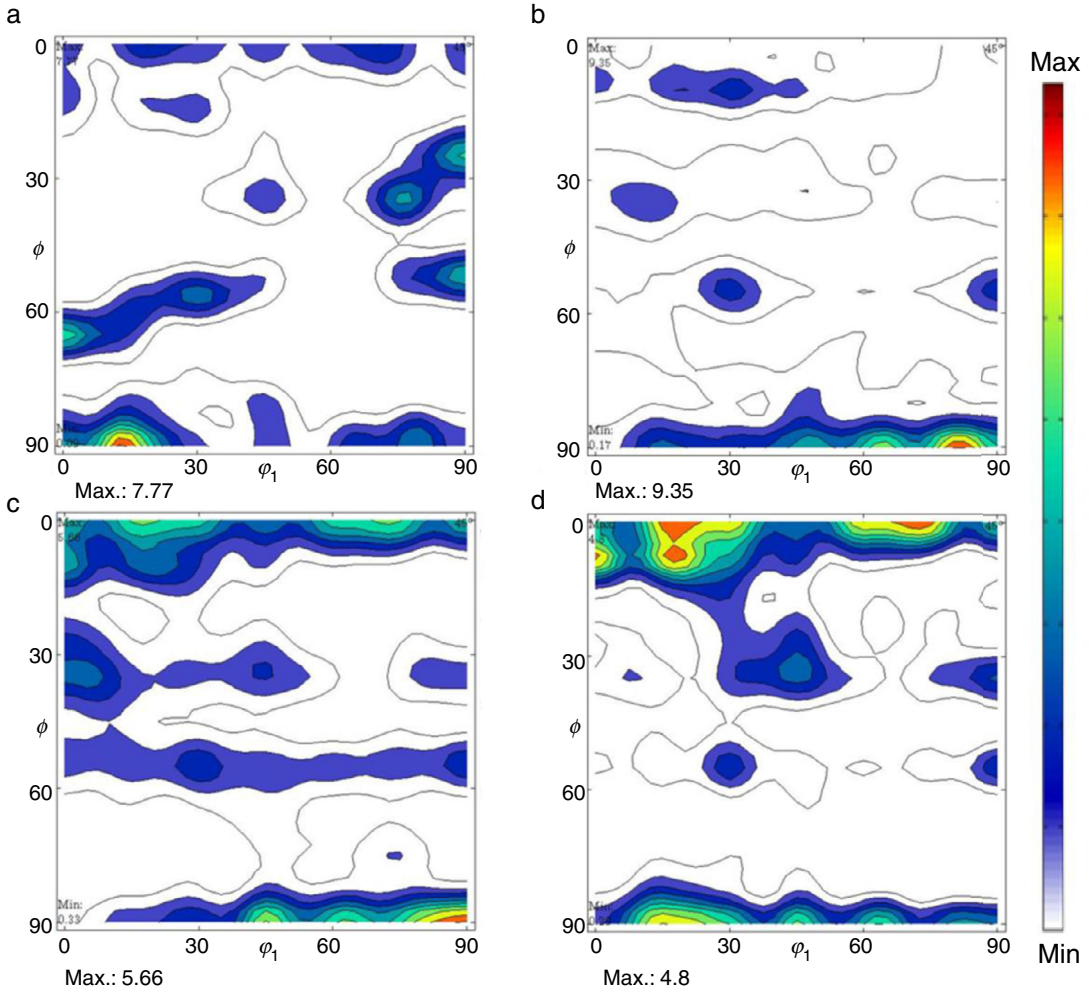

Fig. 4 – ODFs at $\varphi_2 = 45°$, BCC ferrite/martensite texture evolution (a) solution-treated, (b) hot rolled, (c) 50% cold rolled, and (d) 67% cold rolled samples.

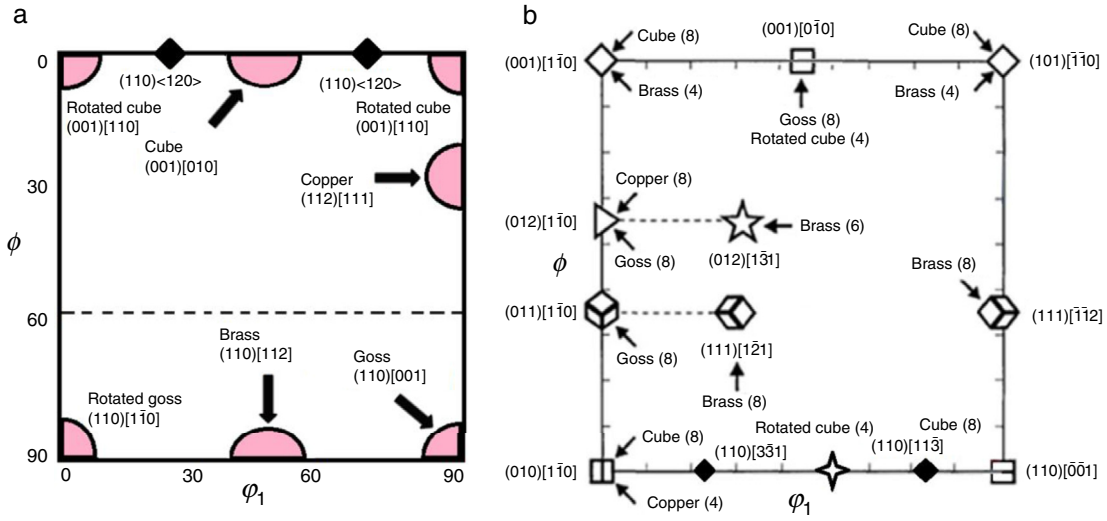

Fig. 5 – Schematic representation of texture component in the $\varphi_2 = 45°$ section between transformation austenite into martensite considering K–S orientation relationship. The figures identify the (a) parent FCC orientation from which a specific (b) BCC orientation originate adopted from [17].

in austenite after deformation. Another texture component of interest is the {113}⟨1$\bar{1}$0⟩ component, which become strongest component in alloys with a low SFE under torsion [20,21]. This implies that the {113}⟨1$\bar{1}$0⟩ component might selectively undergo martensitic transformation similar to the {100}<001> component. According to Fig. 5, the parent austenite component can transform into a BCC Copper component having {113}⟨1$\bar{1}$0⟩ orientation.

3.3. *EBSD studies*

To further investigate the effect of hot and cold rolling, EBSD analyses were conducted in initial, hot-rolled and cold rolled samples. Retained austenite and ferrite can easily be indexed by EBSD technique due to the different crystallographic structure. In contrast, martensitic phase is difficult to identify due to high dislocation density in martensite, which results in poor quality of Kikuchi patterns. During sample preparation the retained austenite near the surface transformed into martensite. Indeed, it was observed that the volume fraction of retained austenite determined by EBSD technique was lower than the amount obtained by XRD. This can be explained by differences in penetration depth between these techniques.

In low carbon content (<0.02%) steel, BCC martensite with low tetragonality is present. Due to the lattice distortion in deformed ferrite/transformed martensite it is difficult to match Kikuchi pattern with undeformed crystal leading to differences in quality of band contrast. Fig. 6a shows band contrast map of cold deformed sample. In the inset image, the frequency distribution of band contrast is shown. One can see that two different peaks are present in this sample indicating separation of undeformed ferrite and deformed ferrite/transformed martensite. This is presented separately in Fig. 6b and c. However, to separate between deformed ferrite and transformed martensite using EBSD technique is not possible.

The EBSD observation of the solution annealed sample indicated the elongated retained austenite was predominantly found at grain boundaries. Microstructure which

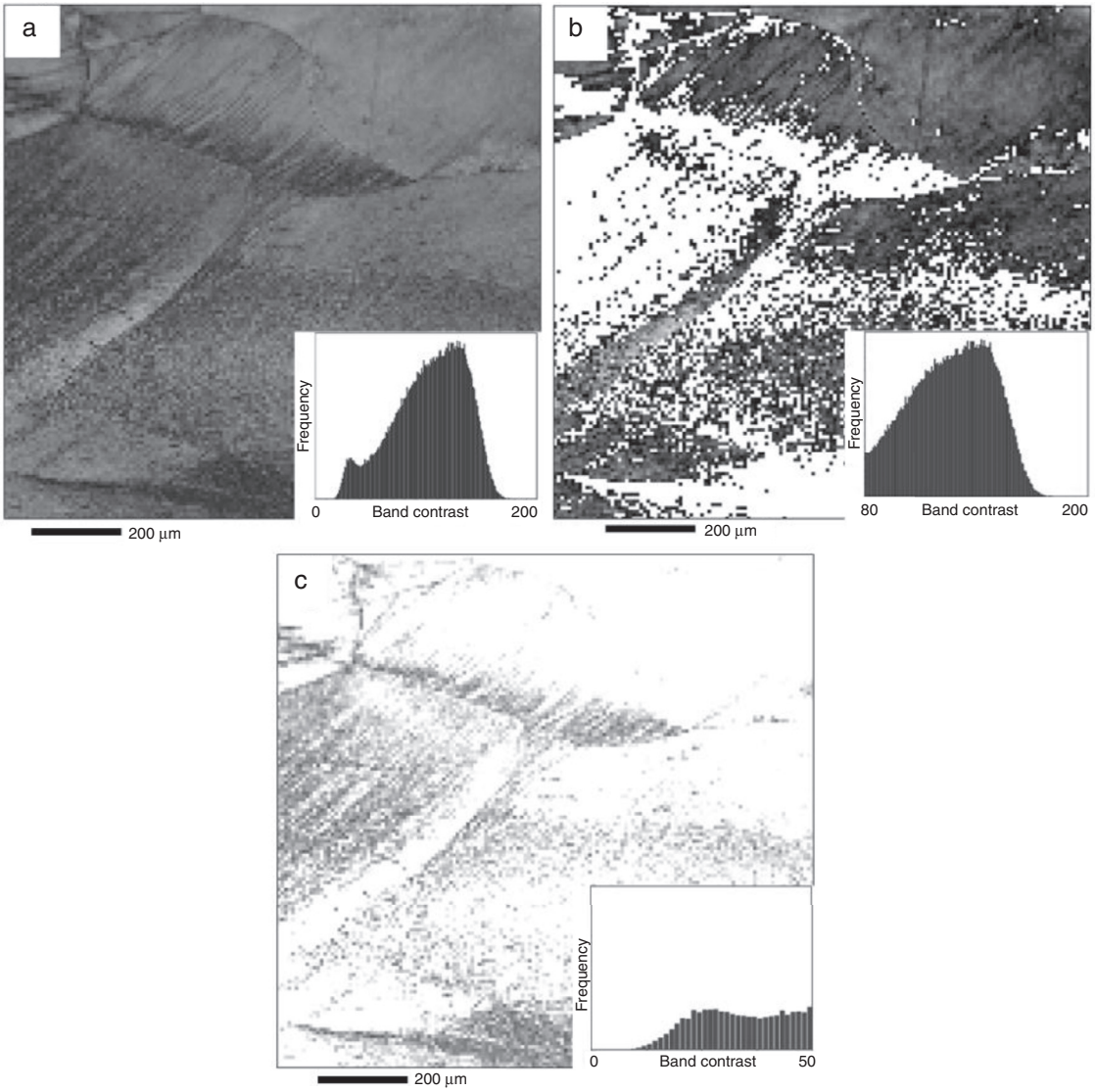

Fig. 6 – Band contrast map of 50% cold deformed sample, (a) EBSD map, (b) ferrite (high band contrast values), and (c) deformed ferrite/transformed martensite (low band contrast values).

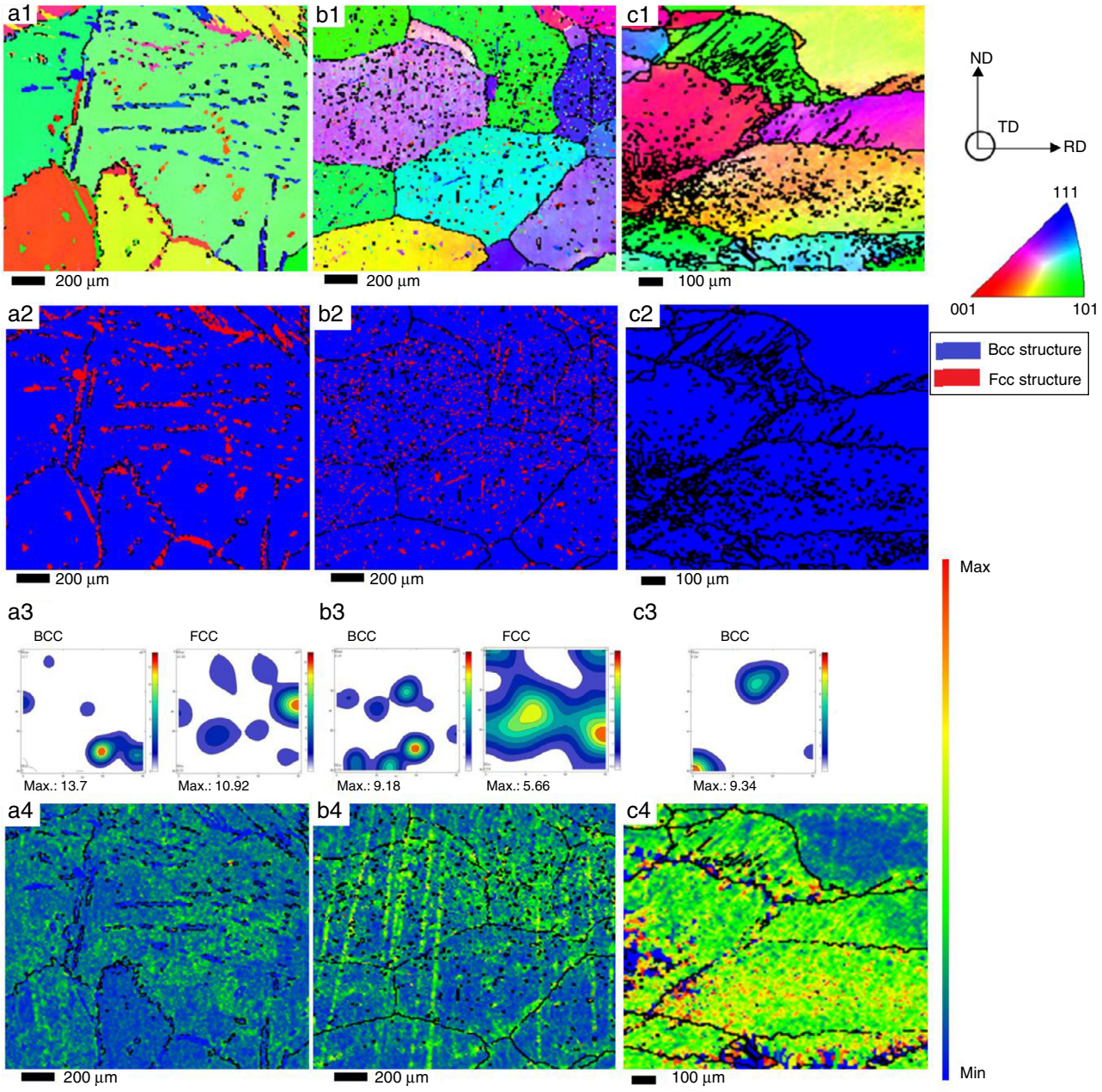

Fig. 7 – EBSD analysis (a) solution-treated, (b) 50% hot rolled, (c) 50% cold rolled. (a1. b1, c1) IPF, (a2, b2, c2) phases identifications, and (a3, b3, c3) related BCC and FCC ODFs, and (a4, b4, c4) KAM.

consists of elongated grains of retained austenite in BCC ferrite/transformed martensite matrix is very beneficial for improvement of the ductility and strength. Higher stresses are applied at the grain boundaries because each grain deforms by different slip system and grain rotation, which induces higher localized stress at boundary. Shen et al. [20] have reported that the mechanical stability of retained austenite is affected by its morphology. The retained austenite is more stable if is surrounded by martensitic phase, which have higher deformation resistance. This martensitic transformation at the grain boundaries could be ascribed to the higher localized stresses. In contrast, if retained austenite is located at grain boundary it exhibits lower stability.

The inverse pole figure (IPF) maps were used to illustrate grain orientations. The ODFs (Fig. 7a3, b3 and c3) of each phase were calculated separately from IPF maps (Fig. 7a1, b1, and c1). The ODF analysis of initial material showed that (112)[111] (copper) (φ_1,ϕ,φ_2: 90,35,45°) component was the main orientation of retained austenite, whereas the (221)[212] (φ_1,ϕ,φ_2: 60,80,45°) was the dominant texture component in ferrite. In hot rolled samples the (332)[113] (φ_1,ϕ,φ_2: 90,65,45°) was predominant in the FCC phase. Ray et al. [21] showed beneficial effect of this texture component for strain induced martensitic transformation leading to improvement of strength and toughness. Also, (111)[101] (φ_1,ϕ,φ_2: 50,75,45°) component was observed in hot deformed sample. In cold rolled samples,

Fig. 7c3, due to shear strain generated between rolls and sheet surface, retained austenite transformed completely and dominant (110)[110] (rotated Goss) (φ_1,ϕ,φ_2: 0,90,45°) texture developed. This suggests that the martensitic transformation is related to the applied shear strain.

IPF maps (Fig. 7a1, b1 and c1) demonstrate that the ferrite grains were coarse and quasi-polygonal in initial condition then decreased gradually with progressing deformation. This trend grain size reduction can be attributed to the increased density of low angle grain boundaries (LAGBs). The misorientation analysis obtained by EBSD demonstrated that the ratio of LAGBs increased from ~35% in initial material to ~85 and ~95% in hot and cold rolled samples, respectively. Then, various deformation bands are formed at grain interior, next dislocations are trapped at subdivide grain boundaries which lead to formation of LAGBs at grain interior as described by Belyakov et al. [22].

Kernel average misorientation (KAM) can be used to monitor dislocation motion including dislocation density inside individual grain during deformation [23,24]. The KAM is represented by the average misorientation between a given point and its nearest neighbor belonging to the same grain and associated with a misorientation less than 15°. An increase in the KAM is closely associated with the cumulative dislocation density. The KAM maps (Fig. 7a4, b4 and c4) obtained from corresponding EBSD maps demonstrates the strain distribution evolution during deformation, where red color indicates highest KAM value. In the solution annealed specimen, the local misorientation was found to be non-uniform distributed where higher intensity was observed near grain boundary regions and was found to be low inside the grain. During hot rolling, the magnitude of the local misorientation increased, while recovery and dynamic recrystallization took place which led to annihilation and reduction of dislocation density. Because of low SFE in austenite, partial recrystallization took place. However recovery was the dominant mechanism in ferrite due to high SFE. In addition the local misorientation increased inside grains and grain boundaries. Micro-bands were formed, indicating that these regions suffered majority of the deformation. In cold rolled sample, the KAM values increased significantly in both at grain boundaries and inside the grains. In this condition, the fraction of high KAM values exceeded 90% and indicated more homogeneous distribution. Furthermore, the retained austenite was completely transformed into martensite. Also, Winther et al. [25] has reported that at higher strain the newly formed martensite have the highest KAM value due to the displacive transformation mechanism. The newly formed martensite has higher hardness in comparison to soft ferrite. In [26] it was demonstrated that crack formation is enhanced by variation in hardness between individual phases. Results obtained in this work can be utilized to enhance precision of material models [27,28].

4. Conclusions

The effect of hot and further cold deformation on microstructure, phase transformation and texture evolution in the experimental 25Cr-6Mo-5Ni stainless steel were investigated. Following conclusions can be drawn:

- The microstructure of solution annealed sample consists of ferrite and austenite.
- With progressing deformation degree at room temperature, the volume fracture of retained austenite decreased from 33 vol.% to 13 and 10 vol.% in 50 and 67% cold rolled specimens, respectively.
- The BCC transformed martensite showed dominant {100}//ND and {110}//ND texture components. The dominance of {100}//ND component was attributed to the martensitic transformation whereas {110}//ND component was induced by shear strain generated between rolls and sheet surface.
- High localized stresses were developed at grain boundaries due to different deformation of individual grains and enhanced martensitic.
- Kernel average misorientation increased significantly with progressing degree of deformation and reduction in rolling temperature.

Conflicts of interest

The authors declare no conflicts of interest.

Acknowledgments

The authors acknowledge the Brazilian research agencies CNPq and CAPEs, the Research Board of the Federal University of Ceará for the financial support and Laboratório de Caracterizaç ão de Mate-riais (LACAM) and Analytical Center (CT-INFRA/MCTI-SISNAD) for the provision of research facilities of this work.

REFERENCES

[1] Sadeghian M, Shamanian M, Shafyei A. Effect of heat input on microstructure and mechanical properties of dissimilar joints between super duplex stainless steel and high strength low alloy steel. Mater Des 2014;60:678–84.
[2] Tan H, Jiang Y, Deng B, Sun T, Xu J, Li J. Effect of annealing temperature on the pitting corrosion resistance of super duplex stainless steel UNS S32750. Mater Charact 2009;60(9):1049–54.
[3] Sarlak H, Atapour M, Esmailzadeh M. Corrosion behavior of friction stir welded lean duplex stainless steel. Mater Des 2015;66:209–16.
[4] Vasconcelos IF, Tavares SSM, Reis FEU, Abreu HFG. Ageing effects on α' precipitation and resistance to corrosion of a novel Cr-Mo stainless steel with high Mo content. J Mater Sci 2009;44:293–9.
[5] Negreiros YS, Herculano LFG, Lima-Neto P, Araujo WS, Guimarães RF, Abreu HFG. Efeito do Teor de Mo na resistência a corrosão de ligas Fe-Cr-Mo. In: Congresso Brasileiro de Engenharia e Ciência dos Materiais – CBECIM; 2008.
[6] Wan J, Ran Q, Li J, Xu Y, Xiao X, Yu H, Jiang L. A new resource-saving, low chromium and low nickel duplex stainless steel 15Cr–xAl–2Ni–yMo. Mater Des 2014;53:43–50.
[7] Ghosh S, Rana VPS, Kain V, Mittal V, Baveja SK. Role of residual stresses induced by industrial fabrication on stress corrosion cracking susceptibility of austenitic stainless steel. Mater Des 2011;32(7):3823–31.

[8] Zaid MD, Bhattacharjee PP. Electron backscatter diffraction study of deformation and recrystallization textures of individual phases in a cross-rolled duplex steel. Mater Charact 2014;96:263–72.
[9] Liu Y, Yan H, Wang X, Yana M. Effect of hot deformation mode on the microstructure evolution of lean duplex stainless steel 2101. Mater Sci Eng A 2013;575:41–7.
[10] Bachmann F, Hielscher R, Schaeben H. Grain detection from 2d and 3d EBSD data—specification of the MTEX algorithm. Ultramicroscopy 2011;111(12):1720–33.
[11] Akdut N, Foct IB. Phase boundaries and deformation in high nitrogen duplex stainless steel. I. Rolling texture development. Scr Metall Mater 1995;32:103–8.
[12] Rastani M. Mechanism of slip and twinning. NCA&T State University; 1992. p. 235–43.
[13] Zaid M, Bhattacharjee PP. Evolution of microstructure and texture during isothermal annealing of a heavily warm-rolled duplex steel. ISIJ Int 2014;54:2844–53.
[14] Bhattacharjee PP, Zaid M, Sathiaraj GD, Bhadak B. Evolution of microstructure and texture during warm-rolling of a duplex steel. Metall Mater Trans A 2014;45:2180–91.
[15] Ahmed M, Bhattacharjee PP. Microstructure, texture and tensile properties of a severely warm-rolled and annealed duplex stainless steel. Steel Res Int 2016;87:472–83.
[16] Bain EC. transactions of the American institute of mining and metallurgical engineers. Iron Steel Div 1933;105:238–58.
[17] Jonas JJ. Transformation textures associated with steel processing. In: Microstructure and texture in steels. Materials engineering. McGill University; 2009. p. 3–18 [Chapter 1].
[18] Tóth LS, Neale KW, Jonas JJ. Stress response and persistence characteristics of the ideal orientations of shear texture. Acta Metall 1989;37(8):2197–210.
[19] Tóth LS, Jonas JJ, Daniel D, Bailey JA. Texture development and length changes in copper bars subjected to free end torsion. Textures Microstruct 1992;19:245–62.
[20] Shen YF, Qiu LN, Sun X, Zuo L, Liaw PK, Raabe D. Effects of retained austenite volume fraction, morphology, and carbon content on strength and ductility of nanostructured TRIP-assisted steels. Mater Sci Eng A 2015;636:551–64.
[21] Ray RK, Chapellier FP, Jonas JJ. Correlations between the rolling textures in fcc Ni-Co alloys and the bcc transformation textures in controlled rolled steels. Textures Microstruct 1990;12:141–53.
[22] Sakai T, Belyakov A, Kaibyshev R. Dynamic and post-dynamic recrystallization under hot, cold and severe plastic deformation conditions. Progress Mater Sci 2014;60:130–207.
[23] Fleck A, Muller GM, Ashby MF, Hutchinson JW. Strain gradient plasticity: theory and experiment. Acta Metal Matér 1994;42:475–87.
[24] Demir E, Raabe D, Zaafarani N, Zaefferer S. Investigation of the indentation size effect through the measurement of the geometrically necessary dislocations beneath small indents of different depths using EBSD tomography. Acta Mater 2009;57:559–69.
[25] Winther G, Jensen DJ, Hansen N. Dense dislocation walls and microbands aligned with slip planes-theoretical considerations. Acta Mater 1997;45:5059–68.
[26] Tasan CC, Diehl M, Yan D, Zambaldi C, Shanthraj P, Roters F, Raabe D. Integrated experimental–simulation analysis of stress and strain partitioning in multiphase alloys. Acta Mater 2014;81:386–400.
[27] Novotný L, Ivančo V. Calculations of phase transformations in welding simulations. Appl Mech Mater Trans Tech Publ 2014;611:46–53.
[28] Halama M, Jerolitsch D, Žilková J, Dzedzina R, Linhardt P. Improvement of ENA-NOCS technique using artificial neural networks approach for the detection of corrosion. Eurocorr 2010:1–8.